JGR Solid Earth

RESEARCH ARTICLE
10.1029/2020JB019445

Key Points:

- A propagating network of hydraulic fractures due to internal fluid production is modeled
- Results indicate three phases including (1) individual fracture growth, (2) fracture coalescence, and (3) overpressure relaxation
- External stress anisotropy controls overall orientation, and local stress redistribution controls coalescence

Supporting Information:

- Supporting Information S1

Correspondence to:
O. Rabbel,
ole.rabbel@geo.uio.no

Citation:
Rabbel, O., Mair, K., Galland, O., Grühser, C., & Meier, T. (2020). Numerical modeling of fracture network evolution in organic-rich shale with rapid internal fluid generation. *Journal of Geophysical Research: Solid Earth*, *125*, e2020JB019445. https://doi.org/10.1029/2020JB019445

Received 17 JAN 2020
Accepted 31 MAY 2020
Accepted article online 3 JUN 2020

Numerical Modeling of Fracture Network Evolution in Organic-Rich Shale With Rapid Internal Fluid Generation

Ole Rabbel[1], Karen Mair[1], Olivier Galland[1], Carina Grühser[2], and Tobias Meier[2]

[1]Physics of Geological Processes, The NJORD Centre, Department of Geosciences, University of Oslo, Oslo, Norway,
[2]geomecon GmbH, Berlin, Germany

Abstract When low-permeability and organic-rich rocks such as shale experience sufficient heating, chemical reactions including shale dehydration and maturation of organic matter lead to internal fluid generation. This may cause substantial pore fluid overpressure and fracturing. In the vicinity of igneous intrusions emplaced in organic-rich shales, temperatures of several hundred degrees accelerate these processes and lead to intense fracturing. The resulting fracture network provides hydraulic pathways, which allow fluid expulsion and affect hydrothermal fluid flow patterns. However, the evolution of these complex fracture networks and controls on geometry and connectivity are poorly understood. Here, we perform a numerical modeling study based on the extended finite element method to investigate coupled hydromechanical fracture network evolution due to fast internal fluid generation. We quantify the evolution of different initial fracture networks under varying external stresses by analyzing parameters including fracture length, opening, connectivity, and propagation angles. The results indicate a three-phase process including (1) individual growth, (2) interaction, and (3) expulsion phase. Magnitude of external stress anisotropy and degree of fracture alignment with the largest principal stress correlate with increased fracture opening. We additionally find that although the external stress field controls the overall fracture orientation distribution, local stress interactions may cause significant deviations of fracture paths and control the coalescence characteristics of fractures. Establishing high connectivity in cases with horizontally aligned initial fractures requires stress anisotropy with $\sigma_V > \sigma_H$, while the initial orientation distribution is critical for connectivity if stresses are nearly isotropic.

1. Introduction

Fracturing of rocks usually involves an interplay between external stresses, for example, tectonics far-field stresses, and pore fluid pressure. In the case of low-permeability sedimentary rocks such as shale, various geological processes may cause the buildup of strong pore fluid overpressure, which eventually leads to natural hydraulic fracturing (Bjorlykke, 2010; Cobbold & Rodrigues, 2007). These geological processes commonly include temperature-dependent chemical reactions such as mineral dehydration, generation of hydrocarbons through maturation of organic matter, or precipitation of minerals in the pore space (Aarnes et al., 2012; Kobchenko et al., 2011; Ougier-Simonin et al., 2016; Townsend, 2018). In otherwise impermeable rocks, the resulting fractures constitute pathways for efficient fluid migration. Therefore, these processes are considered essential for primary hydrocarbon migration, as well as hydrothermal fluid circulation in shale formations (Iyer et al., 2017; Ougier-Simonin et al., 2016; Panahi et al., 2019).

In a standard burial scenario, both hydrocarbon generation and mineral dehydration or precipitation are slow processes that can take millions of years, potentially leading to buoyancy driven (Jin & Johnson, 2008) or subcritical fracture propagation (Jin et al., 2010). The reaction rates can become much faster if magmatic intrusions are emplaced in organic-rich shale. The rapid heating leads to strong overpressure buildup and fracturing throughout the rocks surrounding the intrusion within a few years, or possibly even days or hours (Aarnes et al., 2012; Galerne & Hasenclever, 2019; Panahi et al., 2019).

Figure 1 illustrates this scenario, in which fractures may provide migration pathways for large amounts of hydrocarbon liquids and gases. These can be stored in subsurface reservoirs or emitted into the atmosphere through volcanic vents (Iyer et al., 2017; Spacapan et al., 2020). However, the dynamics of fracture network

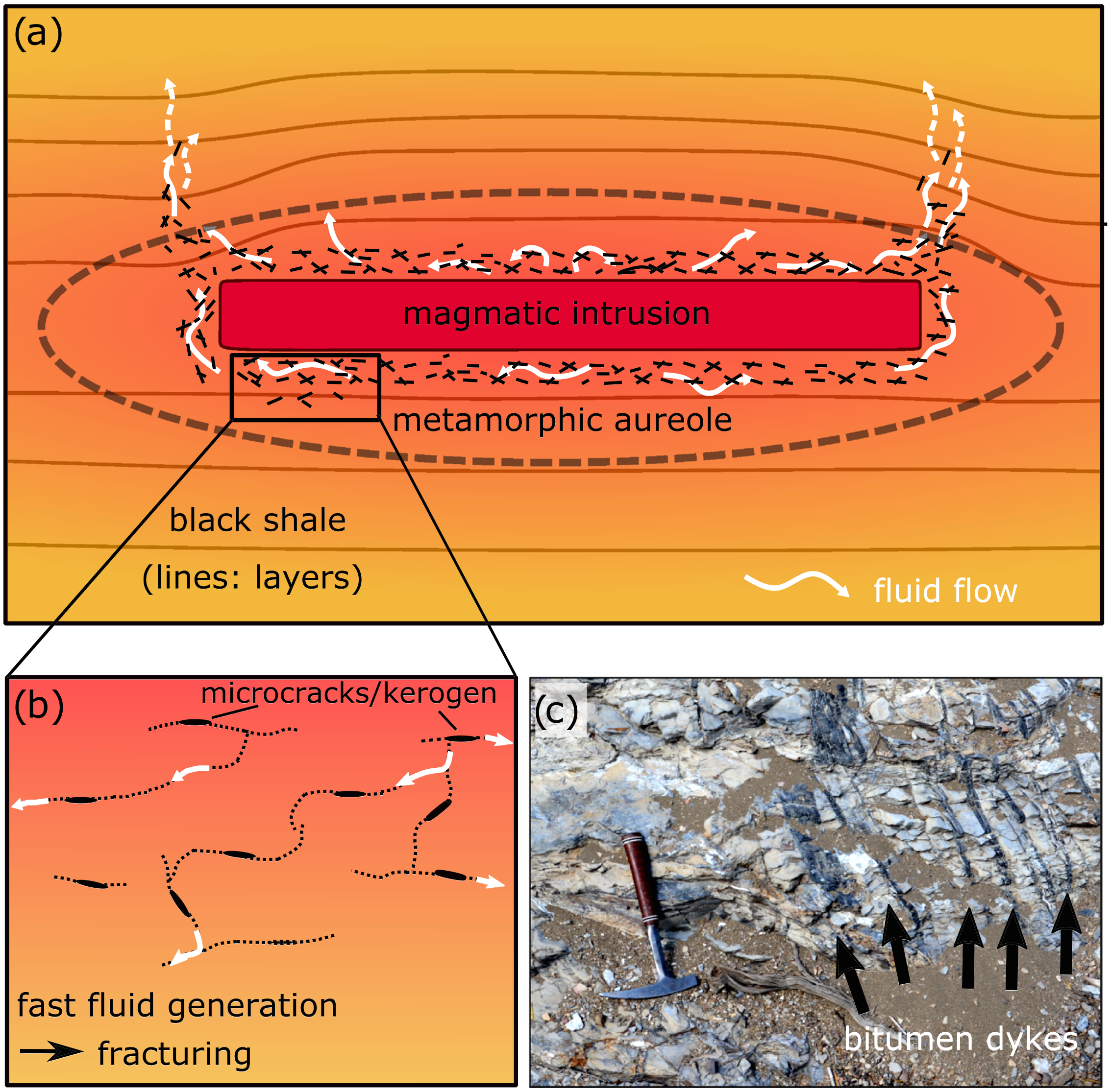

Figure 1. Schematic illustration of the processes related to strong heating of shale due to a magmatic intrusion. (a) Heat from the intrusion creates a metamorphic aureole with high chemical reaction rates. (b) Rapid fluid generation is thought to cause fast overpressure buildup and create a fracture network, which provides migration pathways for fluids. (c) Field example of bitumen dykes in shale matured by magmatic intrusions (Neuquén Basin, Argentina).

growth and its effect on fluid expulsion and transport properties in strongly heated shale are still poorly constrained. Thus, it is crucial to develop a quantitative understanding of the coupling between internal fluid generation and fracture network evolution.

Fractures representing fluid pathways in tight, organic-rich shales are well documented from both field and borehole data in both standard burial and volcanic settings (Marquez & Mountjoy, 1996; Ougier-Simonin et al., 2016; Spacapan et al., 2019; Zanella et al., 2015). However, our current understanding of hydrofracturing due to internal fluid generation stems primarily from laboratory models and a few numerical studies. Typically, the process observed in experiments can be subdivided into three phases, including (1) fracture initiation, (2) growth and coalescence, and (3) expulsion (Kobchenko et al., 2014; Panahi et al., 2018, 2019).

Experiments with heated shale indicate that fracture initiation on the microscale starts from small preexisting flaws that promote stress concentration, such as elliptic pores or kerogen patches in shale (e.g., Figueroa Pilz et al., 2017; Kobchenko et al., 2011; Panahi et al., 2019). Similar fracture initiation mechanisms were observed in analogue experiments using brittle, elastic gelatin-yeast mixtures, where a drainage fracture network developed from elliptic gas bubbles (Kobchenko et al., 2014; Vega et al., 2018). Fracture propagation is thought to be driven by continuous liquid and gas production, and several factors may influence the propagation direction: (1) initial orientation of kerogen flakes or thin pores, for example, due to sedimentary lamination, (2) external stress field configuration, and (3) internal stress interactions (Kobchenko et al., 2011; Panahi et al., 2018; Vega & Kovscek, 2019; Vernik, 1994). Observations linked to fluid and gas expulsion in laboratory experiments include cyclic fluctuations of fracture apertures, that is, opening and closing, in response to fluid pressure buildup and relaxation due to fluid generation and burst-like expulsion (Kobchenko et al., 2014; Panahi et al., 2018, 2019).

Laboratory experiments are limited by time, scale, and cost. Additionally, quantification of the exact stress state during fracture network evolution remains challenging. Therefore, numerical studies represent an important tool to study complex fracture network evolution due to internal fluid generation in organic-rich rocks. To our knowledge, there are only two numerical studies of this type to date (Teixeira et al., 2017; Vega et al., 2018). Teixeira et al. (2017) focused on the influence of differential stresses and initial spacing and size of kerogen patches on the orientation and potential interconnectivity of newly formed microfractures around the patches. Meanwhile, Vega et al. (2018) presented a phase-field method to model systems similar to the gelatin models, establishing good agreement with the laboratory results and linking fracture network characteristics to the elastic properties of gelatin. However, the *evolution* of a fracture network and its relation to the stress state of a medium with internal fluid production has not been investigated thoroughly. To address this issue, we present a two-dimensional (2-D) numerical model study based on the extended finite element method (XFEM) for hydraulic fracturing, which we use to simulate propagation, coalescence, and drainage of multiple fractures due to internal fluid overpressure.

The main goal of our study is to present a workflow to quantify the evolution of fracture network parameters that can be related to the stress state of the coupled hydromechanical model. In this way, we aim to better understand the processes governing complex fracture propagation in organic-rich shale undergoing fast fluid generation due to strong heating and their potential influence on fluid expulsion and migration.

2. Methods

2.1. Modeling Framework

Numerical investigation of the evolution of a fracture network due to internal fluid generation in a rock requires coupling of mechanical deformation and fluid flow in an elastic solid, as well as fracture propagation, interaction, and coalescence. We therefore employ an existing XFEM-based research and development software (geomecon, 2019). XFEM is a popular numerical method used for modeling hydraulic fracture propagation, because it allows the intersection of a finite element mesh by discontinuities, that is, fractures, without the need for time-consuming remeshing (e.g., Belytschko et al., 2009; Fu et al., 2013; Lecampion et al., 2018). The software utilized in this study has previously been applied to investigate fracture network growth and fracture coalescence at the laboratory scale as well as for geotechnical applications (Backers et al., 2012, 2015; Mischo & Backers, 2012; Stöckhert, 2015). It solves the poroelastic formulation of linear elasticity

$$\nabla \cdot (\sigma(\boldsymbol{u})) + \boldsymbol{f} + \alpha \nabla P_p = 0, \tag{1}$$

where $\sigma(\boldsymbol{u})$ denotes stress, α represents Biot's effective stress coefficient (we use $\alpha = 1$), P_p is pore pressure, and $\boldsymbol{f}$ denotes the body force vector. With the help of Darcy's law, spatiotemporal pore pressure variations due to fluid flow and solid deformation are found by solving

$$\frac{\partial P}{\partial t} = \frac{M}{\mu} \nabla \cdot \left(\mathbf{k} \nabla \left(P_p - \rho_f \mathbf{g} \mathbf{x} \right) \right) + \alpha M \frac{\partial \epsilon_b}{\partial t}, \tag{2}$$

where M is Biot's modulus, μ is fluid viscosity, $\boldsymbol{k}$ denotes the permeability tensor, ρ_f is fluid density, $\boldsymbol{g}$ represents gravitational acceleration, and ϵ_b denotes bulk strain. Equations 1 and 2 provide the governing equations required to solve the coupled problem. Here, modeling is restricted to 2-D problems assuming plain strain.

Fracture propagation is implemented as quasistatic, using a combination of Griffith theory for tensile failure and a Mohr-Coulomb criterion for shear failure. This allows the use of reliable rock mechanical parameters (tensile strength, cohesion, and internal friction angle) that are readily available from published laboratory data (Dietrich, 2015; Schön, 2015). The stresses are evaluated in a semicircle around the crack tip, and if tensile or the Mohr-Coulomb failure envelope is exceeded at one or more points on the semicircle, the crack grows in the direction of the most critical stress value. This most critical value is defined as exceeding the critical stress by the largest percentage. If shear and tensile criteria are exceeded by the same amount, by default, tensile failure is realized.

2.2. Model Setup

Figure 2 illustrates our model setup including boundary conditions and geometry. The model includes a 50 × 50 cm square representing a vertical section in the subsurface, assuming plane strain conditions. We subdivide the square into two domains, which we refer to as the "model domain" and the "boundary domain," respectively. The model domain is populated with realistic rock properties for low-permeable organic-rich shale as described in Table 1. Note that although we use isotropic elastic properties and rock strength for simplicity, the modeling software in principle allows for anisotropic parameters. Within the boundary domain, we increased the rock strength and permeability to unrealistically high values, to (1) prevent fractures from connecting to the boundary, thus destroying the mesh and (2) allow drainage of overpressured fractures to the boundary domain upon connection. Elastic and fluid properties are identical in both domains. Fluid viscosity represents an order of magnitude estimate based on water to simulate low-viscosity behavior. In elements cut by fractures, we increase permeability by several orders of magnitude to allow for efficient fluid flow along fractures. This approach will not result in realistic fracture flow but mainly ensures that flow is focused in the fractures. At this time, more realistic, aperture-dependent fracture permeability according to cubic law (Witherspoon et al., 1980) is not implemented. However, we attempt to minimize the error of our approach by using a high-resolution mesh along the fractures.

Figure 2 also shows the predefined fractures in the initial state of the model. We added 25 fractures of 1 cm length in an evenly spaced grid throughout the inner model domain, that is, we omit a simulation of the fracture initiation process and assume that initial, small flaws have already formed. Laboratory studies show that such initial microcracks could form from ellipsoid pores or kerogen flakes (Kobchenko et al., 2011, 2014; Vega et al., 2018).

We start each simulation by pumping fluid into the fractures, which constitute internal model boundaries, at a rate of 5×10^{-9} m^3/s until all fractures start growing. Then, six fracture growth steps (4 mm growth per step) alternate with a single, short (1 s) flow step to allow for fluid pressure relaxation as well as drainage if a fracture connects to the boundary domain. There are several criteria to stop a simulation: (1) After a maximum of 105 calculation steps, that is, 15 growth-flow cycles, (2) all fractures are connected to the boundary domain and have been drained, or (3) all fractures cease growing. Note therefore that since different simulations may fulfill one of the criteria after a different number of computation steps, the simulations have a varying number of total steps.

2.3. Parameter Sensitivity Study

One objective of this study is to investigate fracture network evolution for various external stress states and initial fracture orientations. Therefore, we varied the initial orientation of the fractures in three configurations of increasing alignment with the horizontal axis, choosing a random value within 90°, 45°, and 15° from the horizontal axis, respectively. We refer to these three configurations as "random," "semialigned," and "aligned," respectively. In organic-rich shale, stronger alignment of microcracks with the horizontal axis could be a consequence of sedimentary lamination. For each case of the initial fracture geometry, we ran simulations with increasingly anisotropic stress boundary conditions, representing a constant depth of around 2.5 km. This approximately corresponds to the onset of the oil window as well as an intermediate emplacement depth for intrusions that could cause fast maturation of oil and gas (Spacapan et al., 2018, 2019). Starting from applying isotropic stress of 67.5 MPa along all boundaries, we decrease the horizontal stress by 1%, 5%, 10%, and 200%. We apply constant pore pressure of 25 MPa at the outer boundaries of the model. In a geologic sense, this corresponds to an increasingly extensional stress state at a constant depth with hydrostatic fluid pressure except in the fractures. The extreme case of 200% stress anisotropy is based on the

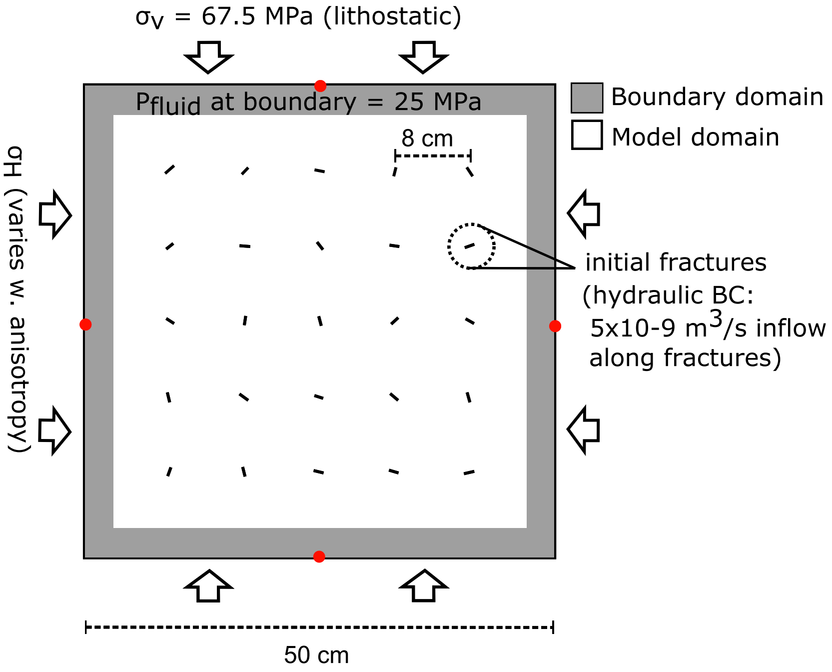

Figure 2. Illustration of the model setup and geometry. Arrows indicate stress boundary conditions, and red dots represent boundary nodes with zero boundary tangential displacement in addition. The inner model domain (white) has realistic physical parameters of shale, while the outer boundary domain (gray) has unrealistically high rock strength and is highly permeable to stop fracture growth and allow drainage.

theoretical consideration of an elastic medium with Poisson ratio of 0.25 under pure vertical compaction with no horizontal strain (e.g., Cobbold & Rodrigues, 2007). Since this case is somewhat unrealistic and mainly designed to give an extreme reference scenario, we mainly focus on the transition from isotropic to a mildly extensional stress state.

2.4. Quantification of Fracture Network Evolution

Presenting an approach to quantify the fracture network evolution and drainage dynamics is another important objective of this work. Accordingly, we extract specific parameters that describe the dynamics of fracture growth and potentially identify different phases, and characterize the connectivity of the final fracture pattern. As illustrated in Figure 3, the parameters include (1) total fracture length of the fracture network, (2) total fracture area, that is, aperture integrated along each fracture, (3) fracture propagation angle with respect to the horizontal, and (4) connections per line. Below, we will describe each parameter in more detail.

Table 1
Rock and Fluid Parameters Used for the Model

Parameter	Value (unit)
Permeability[b]	10^{-20} m^2
Fractures	10^{-12} m^2
Young's modulus[b]	23.9 GPa
Poisson's ratio[b]	0.17
Angle of internal friction[b]	0.543
Cohesion[b]	33.8 MPa
Tensile strength[c]	3 MPa
Biot's modulus[a]	10^{10} MPa
Pore fluid viscosity	10^{-3} Pa·s

Note. Mechanical properties represent averages of literature values, while for permeability, the lowest values were chosen to allow overpressure buildup.
[a] Based on Cosenza et al. (2002). [b] Based on Dietrich (2015). [c] Based on Schön (2015).

First, we monitored the total fracture length from each step, which is straightforward using the resulting fracture node coordinates. In addition, we extracted the total fracture area per simulation step to identify trends in opening and closing of fractures during growth and drainage. Since the coordinates of the fracture nodes and the associated displacement on each side of the fracture are known for each calculation step, it is straightforward to construct open fractures as polygons and measure their area, which corresponds to fracture opening (gray area in Figure 3. Thus, we will use the terms fracture area and opening synonymously.

To measure the trends in the evolution of the fracture orientation, such as alignment with external stresses, we measured the median angle of all new crack elements with respect to the horizontal axis for every simulation step (see Figure 3; hereafter referred to as

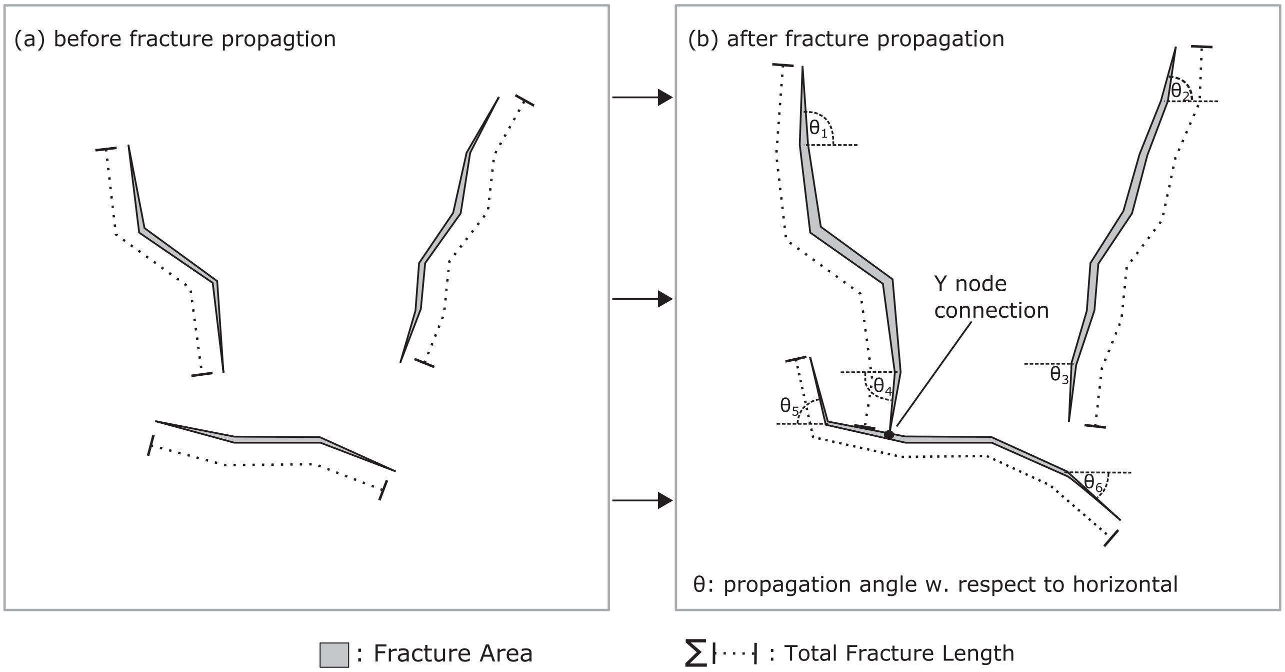

Figure 3. Schematic illustration of the quantities used to characterize fracture network evolution in this study. After each propagation step (from a to b), we calculate the fracture area (gray), total fracture length (sum of all fracture segment lengths), the angles of new fracture segments with respect to the horizontal, and the number of new connection nodes.

"propagation angle"). Due to the relatively small number of fractures in the model, we favor median over arithmetic average, since alignment trends are represented more clearly as median. To relate the evolution of the crack tip orientation to a physically relevant parameter, we plot the propagation angle against ratio of average fracture length to initial fracture spacing (around 8 cm in our case, cf. Figure 2). When this parameter approaches a value of 1, the average fracture length is approximately equal to initial fracture spacing, indicating that fracture interaction may play a role.

The connectivity of the drainage fracture network, in terms of both its evolution and final state, is of particular interest, since even closed fractures could be reopened by renewed pressure buildup as preexisting weaknesses. Here, we use the average number of connections per line C_L to quantify connectivity, which is a dimensionless parameter derived from fracture network topology (Sanderson & Nixon, 2018). C_L is calculated from the number of fracture lines (N_L) connecting nodes between fractures, that is, abutting (N_Y) and crossing (N_X) nodes as

$$C_L = 2(N_X + N_Y)/N_L. \tag{3}$$

While values of $C_L < 2$ indicate a fracture network with limited connectivity, $C_L > 3.57$ has been shown to be the percolation threshold where the entire fracture network is interconnected (Sanderson & Nixon, 2018). Note that in this study, we are analyzing a network with very few fractures and idealized initial positions of the fractures. Therefore, we are mainly interested in the relative connectivity trends of the simulations.

3. Results

3.1. Visualization of the Evolving Fracture Network

Figures 4–6 show time series snapshots for three different modeling cases representing the endmembers of the parameter study. These endmembers include random initial orientation under isotropic external stress (Figure 4), random initial orientation under 10% extensional stress anisotropy (Figure 5), and horizontally aligned initial fractures under 10% extensional stress anisotropy (Figure 6). Each figure consists of four snapshots displaying the state of the fracture network at the same four computation steps, representing various

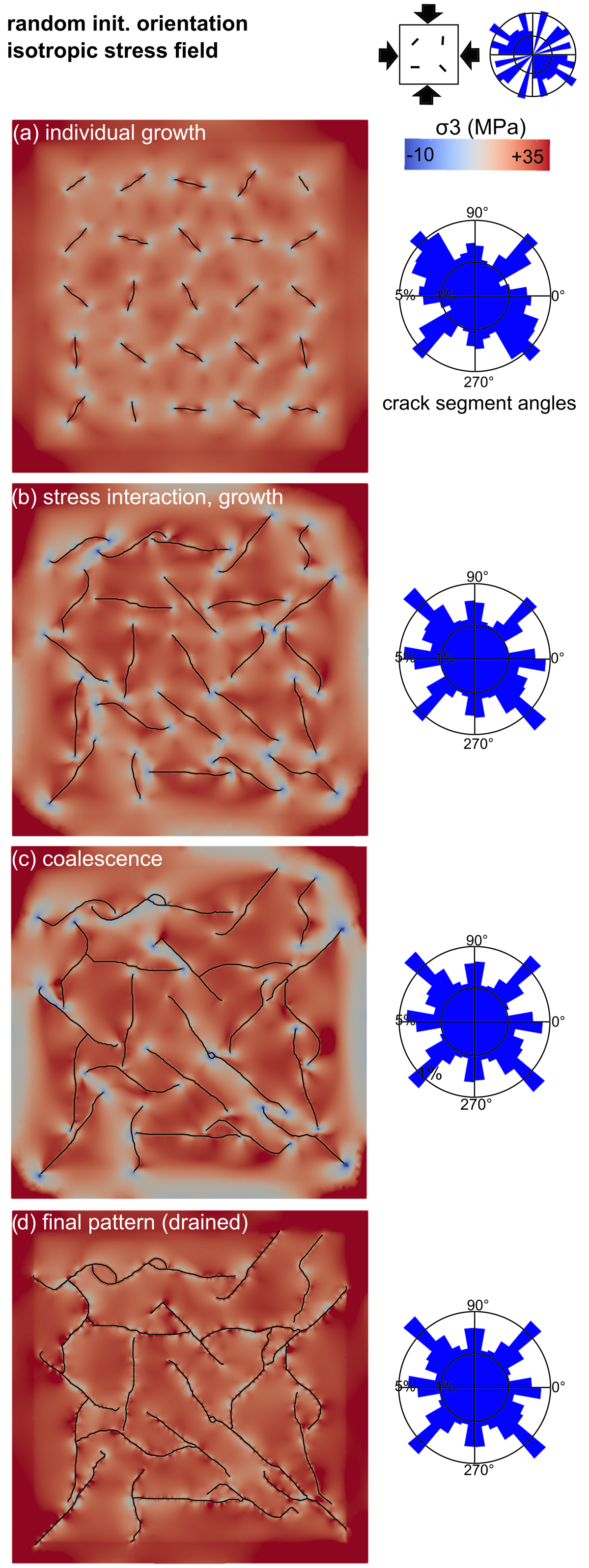

Figure 4. Time series of the fracture network evolution for random initial fracture orientation and isotropic external stress field, along with rose diagrams of all fracture segments for each step. Color code represents the smallest principal stress. Description of the phases (a–d) is given in the text.

development phases. The respective phases include individual (noninteractive) growth, stress interaction, fracture coalescence, and the final fracture pattern at the last computation step. The background color represents the smallest principal stress, with blue color corresponding to tensile stresses and red color corresponding to compressive stresses. For each snapshot, we additionally provide the corresponding orientation distribution of all fracture segments (one segment is defined by two nodes in the mesh) as a rose plot.

For the fracture network with random initial orientation developing under isotropic external stress, we mainly observe growth in the direction of the initial fractures in the individual growth phase (Figure 4a). When stress interactions between the fracture start to become significant, the direction of propagating fracture tips starts to deviate from the earlier paths. In particular, crack tips approaching each other are first deviated to opposite sides and then "embrace" each other, while fracture tips growing toward an open fracture surface deviate following a more orthogonal path toward that surface (Figure 4b). Fractures located near the edges of the model tend to grow toward the edges, which is likely a numerical boundary effect. As the fractures become longer, tensile stresses around their tips intensify. When the fractures start to interconnect in the coalescence phase, the connected tips lose their tensile tip stresses (Figure 4c). However, the stress state of the model is highly heterogeneous, with both highly compressive and tensile areas, especially when compared to the early phase. A visualization of the complexity of coalescence-related stress reconfigurations captured by the model is available in supporting information Figure S1. The final pattern shows a highly interconnected fracture network, which is connected to the boundary domain and therefore drained (Figure 4d). The displayed stress field is much more homogenous and purely compressive. For a better impression of the coupling between fracture drainage, opening/closing, and stress redistribution, we refer to Figure S2.

In the case with random initial orientation and 10% anisotropic extensional stress (Figure 5), we observe some differences compared to the previous case. During the individual growth, most fractures continuously turn toward the vertical direction, which is the direction of maximum externally applied stress (Figure 5a). This trend continues, until the fractures start interacting. We observe that the predominant type of interaction and coalescence is the previously described behavior of fracture tips "embracing" each other upon connection (Figures 5b and 5c). The fracture orientation distribution indicates that the connected fracture network is preferentially aligned in the vertical direction. The connected fracture arrays cause intense stress concentrations around them prior to drainage, creating zones of high compression around them and zones of extension close to the vertical model boundaries. In the final, drained model, the tensile stresses are relaxed and the entire model is under compression (Figure 5d).

The fracture network developing from initially aligned fractures (Figure 6) is characterized by an early growth phase where fractures first grow in an oblique path before turning to the vertical direction (Figure 6a). When the fractures start interacting and finally coalesce, they build fracture pathways that overall connect vertically but appear distinctly more tortuous compared to the previous case (Figures 6b and 6c).

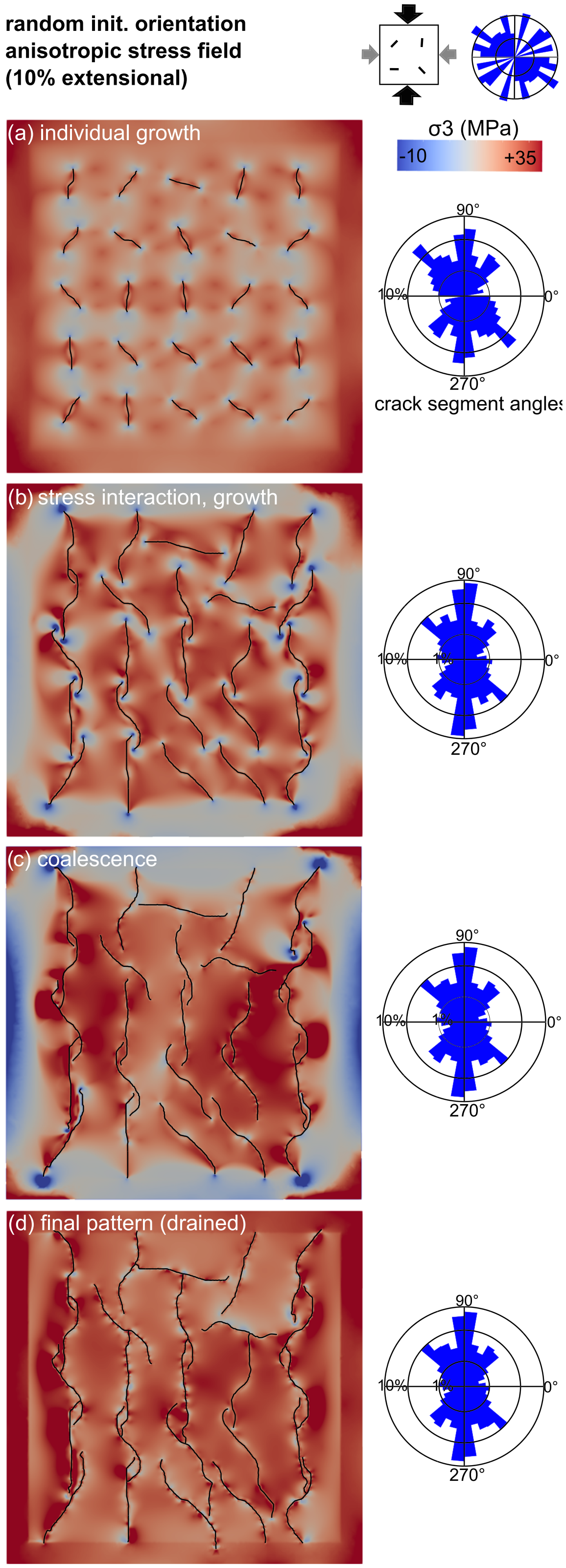

Figure 5. Time series and rose plots of the fracture network evolution for random initial fracture orientation and anisotropic stresses (10% extensional). The color code represents the smallest principal stress. Description of the phases (a–d) is given in the text.

This is expressed in the rose diagrams, which show similar numbers of oblique and vertical fracture segment orientations. Again, tensile stresses due to fluid overpressure disappear after drainage (Figure 6d).

3.2. Quantification of the Fracture Network Evolution

3.2.1. Total Fracture Length

Plotted against computation steps, the total fracture length follows a similar curve in all cases (Figure 7). Starting with linear growth until approximately Computation Steps 35–40 when all fractures propagate at both ends (gray domain, Figure 7), the increase in fracture length is continuously reduced afterwards until almost no growth is visible from around Step 50, when the most fractures have connected to each other or been drained upon connection to the boundary domain (white domain, Figure 7). While both the transition points between fracture growth phases and the values for the total fracture length are very similar for all stress anisotropy values in Figure 7a, we observe that the onset of the late phase of reduced growth is later for stronger initial alignment. Additionally, the final fracture network is characterized by larger total fracture length values for increasing initial alignment (Figure 7b).

3.2.2. Total Fracture Area (Opening)

As illustrated in Figure 8, the total fracture area develops in three distinct phases and additionally shows trends for varying stress anisotropy and initial fracture alignment. Each fracture propagation step usually leads to an increase in the total fracture area, while each decrease of the fracture area corresponds to a flow step associated with some pore pressure relaxation or even complete drainage in the later stages. This makes it easy to identify fluid flow steps in the presented data. Generally, the first phase, up to Computation Step 25, includes mild opening of the fractures during early fracture growth (dark gray background in Figure 8). Until around Calculation Step 40, the curves become increasingly steeper and the evolution of the fracture area diverges clearly for different simulation cases (light gray). In this second phase, we observe first coalescence, boundary domain connection, and drainage events, indicated by the letters C, B, and D in Figure 8. The third phase includes a strong, stepwise decrease in fracture area at each fluid flow step, leading to subsequent drainage and closure of the fractures (white). To illustrate the direct connection between the onset of fluid expulsion and the reduction in fracture area, we refer to a summary of the expulsed fluid volume given in Figure S5.

Although we are able to identify these general phases in all simulations, the individual evolution shows distinctions, particularly in the second and third phases, that is, during phases of fracture coalescence and drainage. For random initial orientation, an isotropic external stress field (black curve in Figure 8a) leads to much smaller growth in total area compared to 5% and 10% stress anisotropy, and the main reduction in open fracture area is distributed over different steps. The case of 10% extensional stress anisotropy is characterized by a very steep increase, and even though the first drainage event happens earlier compared to the other two cases (Calculation Step 36), this drainage step does not lead to a reduction in total fracture area. The second drainage step in this case, however, is associated with a dramatic decrease in fracture area, after which the total opening is actually smaller than in the other cases.

Figure 8b shows the effect of increasing horizontal alignment of the initial fractures. The blue curve is identical to that in Figure 8a, and we observe

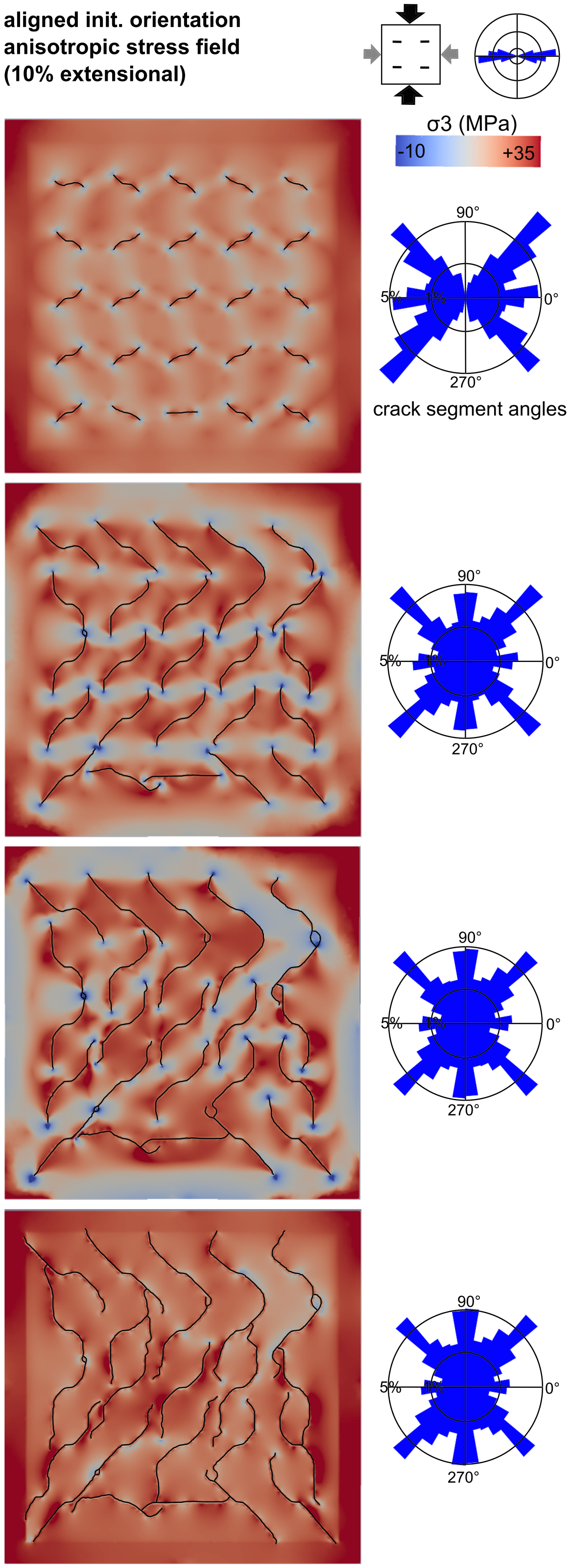

Figure 6. Time series of the fracture network evolution and its orientation distribution for initially aligned fractures in an anisotropic stresses (10% extensional). The color code represents the smallest principal stress. Description of the phases (a–d) is given in the text.

subsequent reduction of the maximum total fracture area with increasing alignment. In the semialigned case (yellow curve), we observe some variations during the phase of strong opening that are related to connecting fractures rather than fluid flow, followed by a strong decrease after the first drainage event. The open fractures of the aligned case (green curve) close over the course of several steps rather than a single event.

3.2.3. Propagation Angles

The evolution of the median angle of propagated fracture segments is illustrated in Figure 9. We display it as a function of the ratio of average fracture length to initial fracture spacing to have a proxy for the distance between fractures. Again, we recognize distinct phases. With the exception of isotropic external stress, the first phase reflects continuous alignment of propagating fractures with the vertical axis, corresponding to the maximum far-field stress direction. The degree of vertical alignment increases from none to a median propagation angle of around 80° when increasing stress anisotropy from 0% to 10% (Figure 9a). For constant 10% stress anisotropy, the median propagation angle reaches around 80° in all cases, but this maximum is reached at a higher average length value (Figure 9b). At a ratio of average length to initial spacing of around 1.1–1.4, the median propagation angle starts to decrease again and reaches values as low as 50°. For increasing initial alignment of the fractures, this minimum value is again shifted toward higher values of average length versus initial spacing. Finally, the curve becomes chaotic and average length does not increase significantly anymore, because of the reduced number of propagating crack tips. Note that Figure S3 provides additional information for all cases in the form of boxplots representing the shape of the propagation angle distribution. We find the observed shift in median angle is in fact an expression of a shift toward more vertical propagation angles for nearly all propagating fractures. In all cases with strongly anisotropic external stress, 75% of the fracture propagates at 60° or larger angles near the maximum of the median propagation angle (Figure S3).

3.2.4. Connectivity (Connections per Line)

We use measurements of average connections per line (C_L) to trace the evolution of connectivity in the fracture networks (Figure 10). In all simulations, the values stay at low values until around Calculation Step 30, when the first individual fractures coalesce. Such connection events cause the vertical steps seen in the connectivity curves.

For initially random fractures, we find that decreasing the differential stress leads to a systematic increase in fracture connectivity (C_L) from 1.2 for 10% stress anisotropy, 1.3 for 5% stress anisotropy, to 1.8 for the isotropic case (Figure 10a). Note that C_L does not capture anisotropy in the connectivity, although we do observe this anisotropy qualitatively (cf. Figures 4d and 5d for visualization of the respective final fracture networks). The isotropic case also exhibits the largest number of connection events.

The sensitivity of connectivity to increasing initial alignment is less obvious in our results (Figure 10b). With 10% stress anisotropy applied, the semialigned case shows highest connectivity ($C_L = 1.6$), while initially random fractures lead to the lowest values. The spread of values is slightly smaller than in Figure 10a). Figure 11 presents a summary of the final connectivity value for all combinations of stress anisotropy and initial fracture orientation tested in this study. For random initial orientation and no or small stress anisotropy (<5%), we observe a peak in fracture

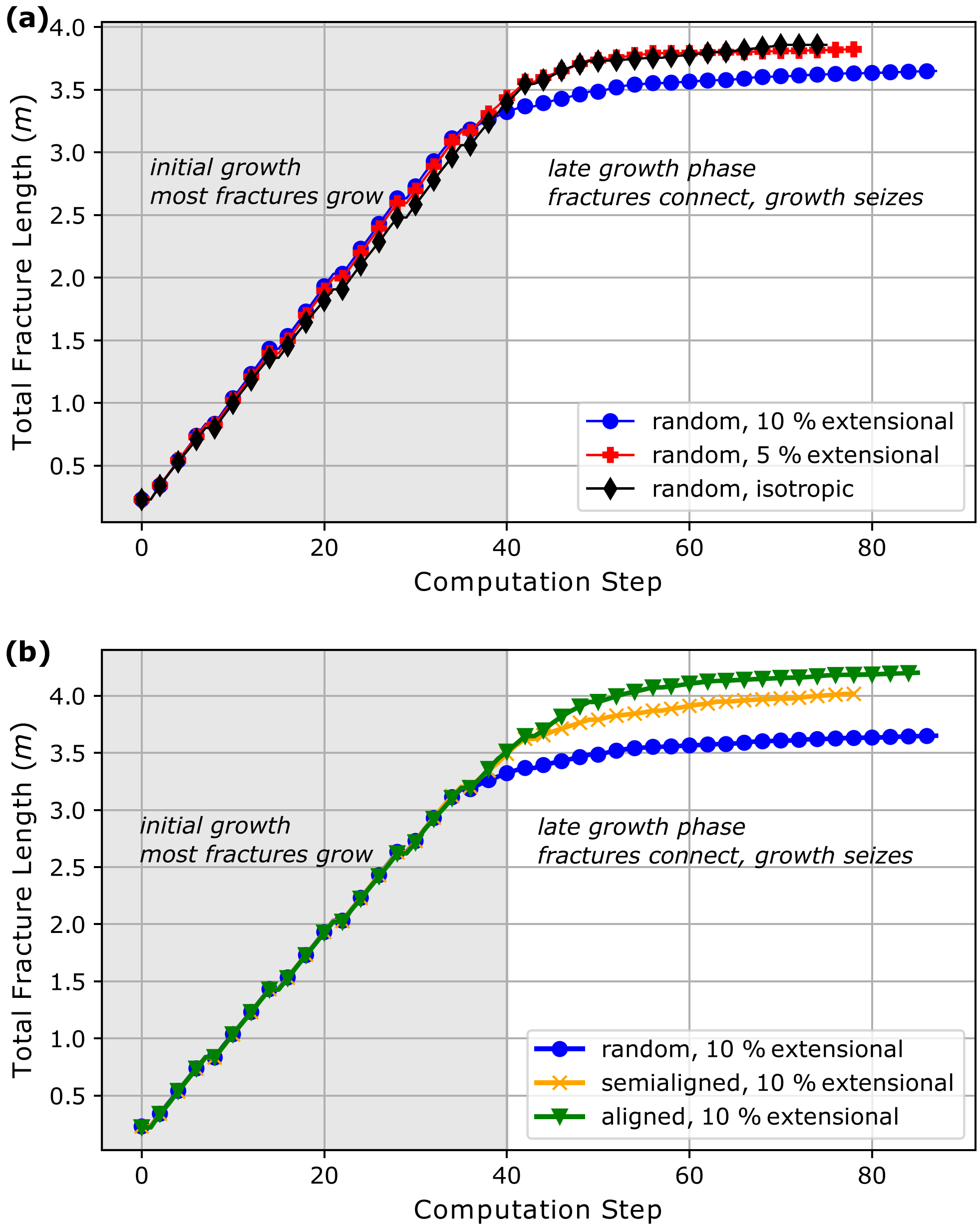

Figure 7. Total length of the fracture network for varying degrees of extensional stress anisotropy for an initially random fracture orientation (a) and varying initial fracture orientations at a given differential stress (10% extensional) (b).

connectivity. Increasing alignment of initial fractures is accompanied by a shift of the maximum value to 5% stress anisotropy, with low connectivity values at both isotropic and strongly anisotropic external stress.

4. Interpretation

4.1. Distinct Phases of the Fracture Network Evolution

We interpret the fracture network evolution in our models to be divided into three phases: (1) early phase of individual fracture growth, (2) intermediate phase of fracture interaction and initial coalescence, and (3) late phase of coalescence, fluid expulsion, and closure of the fractures.

During the early phase (until around Calculation Step 25), the propagation characteristics of individual fractures can be understood using simple fracture mechanics principles. Fluid pressure in all fractures is

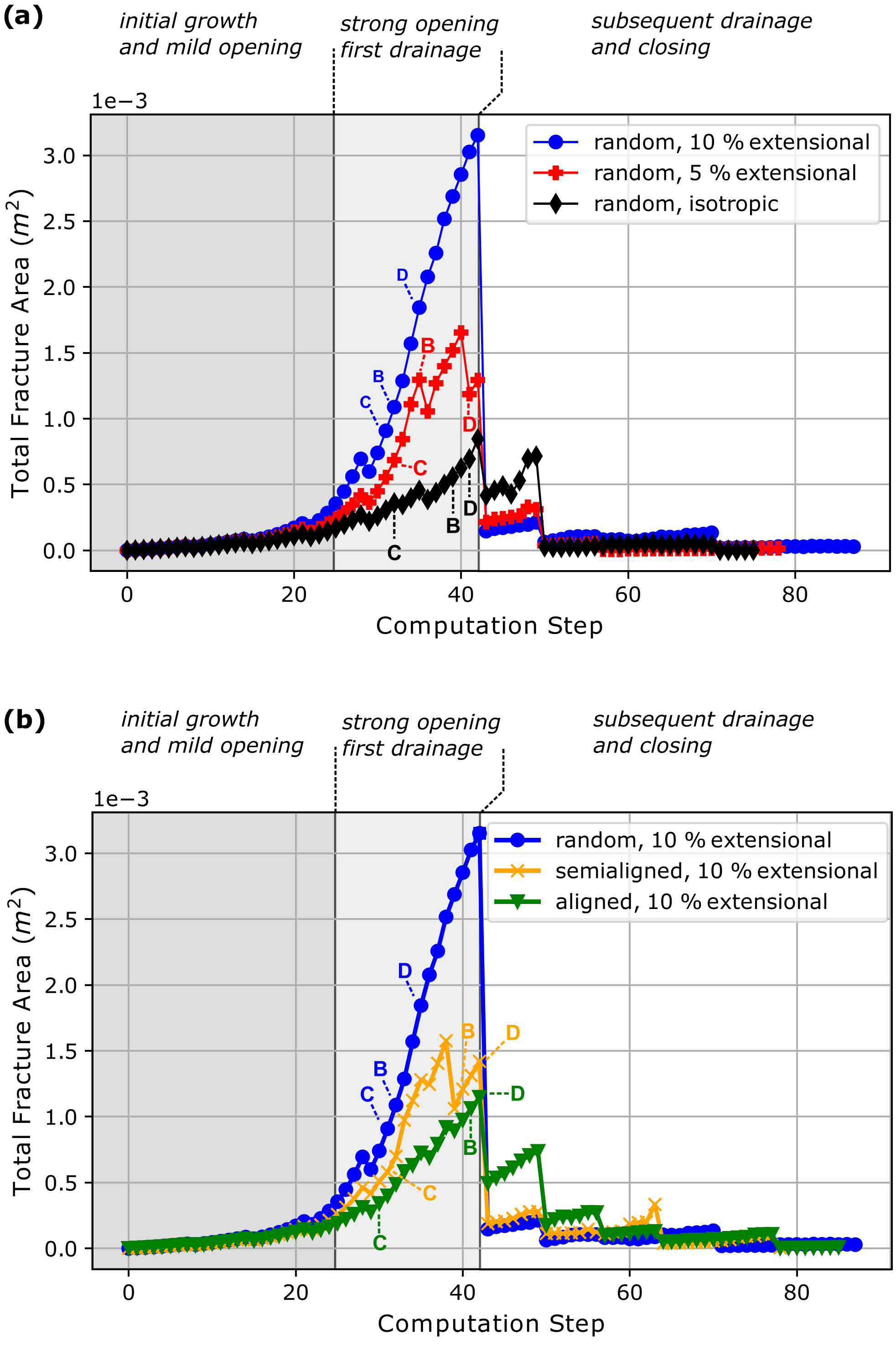

Figure 8. Total fracture area (aperture), for varying degrees of extensional stress anisotropy for an initially random fracture orientation (a) and varying initial fracture orientations at a given differential stress (10% extensional) (b). The letters C, B, and D mark the calculation step number for the first coalescence, boundary domain connection, and drainage event, respectively.

sufficient to cause tensile propagation of all fractures, leading to a linear increase in total fracture length (Figure 7). While the increase in fracture area is small (Figure 8), the early growth phase is the stage in which the dominant orientation of the fractures is established. For low stress anisotropy (<5%), initial

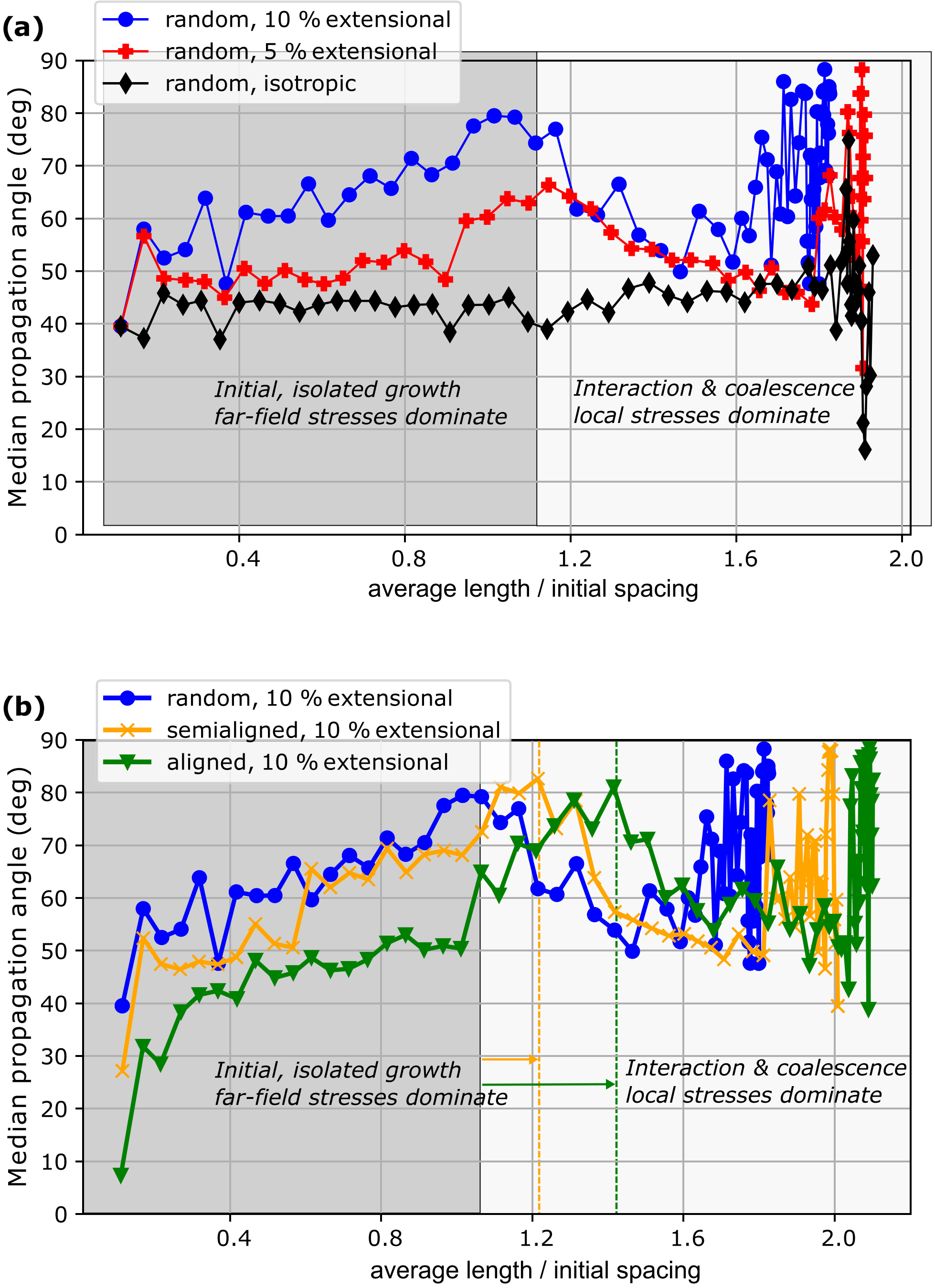

Figure 9. Median propagation angle with respect to the horizontal versus the ratio of average fracture length to the initial spacing. (a) Increasing differential stress from 0% (isotropic) to 10% extensional. (b) Comparison of random, semialigned, and aligned initial crack orientation for a 10% extensional stress configuration.

fracture orientation dominates the orientation of fracture propagation, while increasing differential stress leads to progressive alignment of propagating fractures parallel to the maximum external stress direction (Figures 9 and S3).

The second phase (until approximately Step 40) is characterized by the onset of stress interactions between growing fractures and initial coalescence, as well as a strong increase in fracture area. The interaction of stress fields of different fractures is clearly visible in Figures 4b, 4c, 5b, 5c, 6b, and 6c. Jumps in connectivity indicate coalescence events, because the longest fracture path length increases (Figure 10). The deviation of

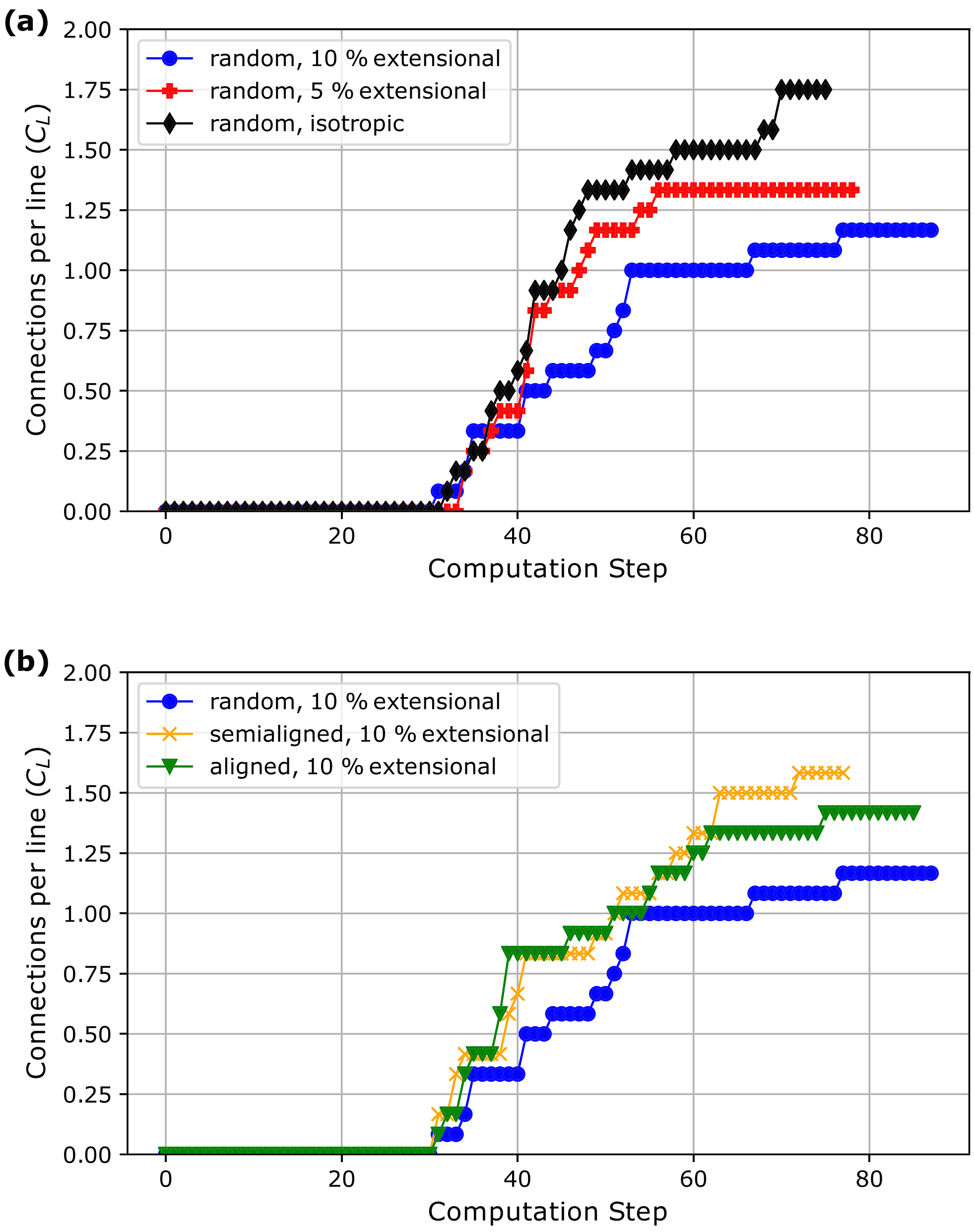

Figure 10. Development of fracture network connectivity (connections per line, C_L). The curves correspond to increasing differential stress (extension) for random initial fracture orientation (a) and increasing initial fracture alignment for an extensional stress field (b). For the random initial configuration, we observe a decrease in connectivity for increasing stress anisotropy (a), while variations in initial alignment do not show a clear trend (b).

propagation angles from their initial trend of alignment with maximum stress direction correlates with the ratio of fracture to initial spacing becoming significantly larger than 1 (Figure 9). Since this ratio expresses a high fracture density and indicates that fractures are likely approaching each other, we argue that the shift in the propagation angle trend is caused by the dominance of local stress interactions over far-field stresses. As an additional identifier, the fracture area increases along a much steeper curve compared to the previous phase, and the curves for the various cases of stress anisotropy start to diverge significantly (Figure 8). We will address the controls on fracture area for the various cases in a later section. Note that the total fracture length (Figure 7) is largely insensitive to this part of the fracture network evolution, highlighting the need for utilizing different parameters.

The final stage comprises further coalescence events that establish the final connectivity as well as the drainage and closure of the fractures. The combination of drainage-related stress relaxation and coalescence

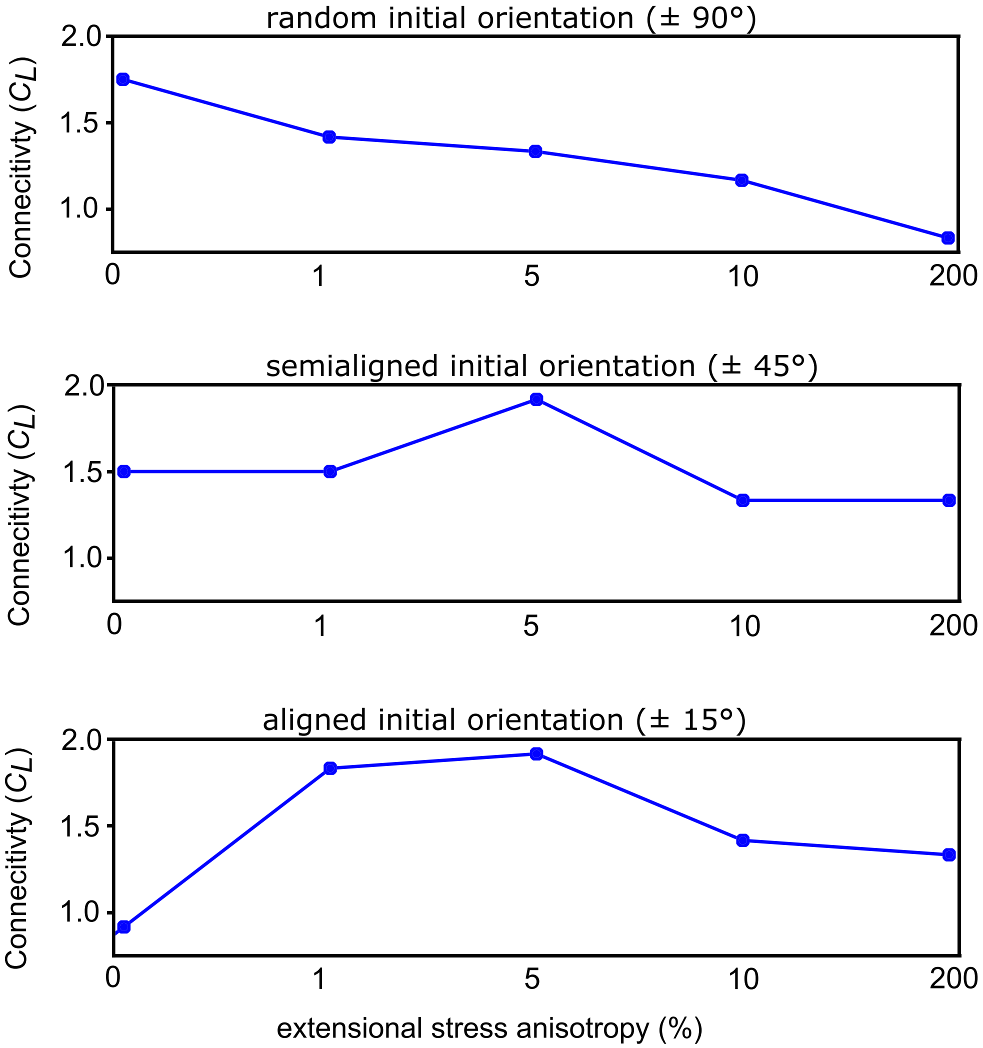

Figure 11. Summary of final connectivity in terms of average connections per line (C_L) for all initial orientations and stress states. For a random initial orientation, increasing extensional stress anisotropy results in subsequently lower connectivity. A connectivity peak at 5% stress anisotropy characterizes the semialigned and aligned cases.

events (steps visible in Figure 10) leads to a strongly decelerated growth in total fracture length (Figure 7), since fewer fracture tips are available for propagation. Due to the decreasing number of propagating fracture tips, the statistics of propagation angles become highly chaotic (Figures 9 and S3). The strong, stepwise reduction of fracture area during flow calculation steps is a result of drainage events resulting from connection of fractures to the boundary domain. The onset of fluid flow through the boundary of the model domain supports this interpretation (Figures S4 and S5). By the end of each simulation, the fracture area has returned to its initial value, implying that all excess fluid pressure has been released from the fractures (Figure 8). This also explains the transition to an entirely compressional and relatively homogenous stress state throughout the model (Figures 4c, 4d, 5c, 5d, 6c, and 6d). Note that due to the permanently established high-permeability connection of fractures to the boundary domain, renewed pressure buildup and fracture opening is not possible.

To sum up, we interpret each simulation to represent a cycle encompassing initial fracture growth, followed by subsequent interaction and coalescence, and finally fluid overpressure relaxation (expulsion) and fracture closure. The interpretation and relation to the stress state of the model is only possible through a combination of various parameters and visualization of the stress state of the model.

4.2. Factors Affecting Fracture Area (Opening)

One of the measured parameters presented in this study that goes beyond typically presented fracture network characteristics is the fracture area, or opening. Since the width of an open fracture severely affects its transport properties, this parameter is particularly interesting. Figure 8 shows two clear trends for the relative scaling of fracture areas during the main phase of fracture growth, especially in the second phase prior to main drainage: (1) Stronger differential stress leads to larger fracture area, and (2) stronger initial alignment of fractures orthogonally to the largest external stress direction leads to smaller fracture area.

Generally, larger normal stress acting on fracture surfaces leads to progressive closing of fractures and vice versa (e.g., Jaeger et al., 2009). Since we create stress anisotropy by reducing horizontal stress in order to simulate different scenarios at the same depth, we can expect fractures in more anisotropic stress fields to show higher fracture area values. Note that this also means that the depth of investigation, that is, changing vertical stress, will also affect opening. However, the different simulations only diverge significantly during the second phase, that is, after initial growth. Thus, an additional factor is needed to explain the large differences between scenarios. The vertical alignment of the fractures is much stronger for larger differential stresses (Figure 9a, cf. Figures 4 and 5). Considering an anisotropic stress field, fractures oriented more toward the direction of maximum stress experience less normal stress on their surfaces. Thus, we argue that it is the combination of preferential alignment and reduced horizontal stress that causes the differences in fracture area in the cases displayed in Figure 8a. The decrease in fracture area with stronger horizontal alignment of initial fractures (Figure 8b) can also be explained by the overall orientation distributions of the fracture segments. In the aligned case, the fracture network includes many subhorizontal fracture segments in its highly tortuous fracture paths (cf. Figure 6), which experience stronger normal stresses due to vertical σ_1.

Furthermore, the temporal evolution of the fracture opening is influenced by fracture coalescence and drainage. Since coalescence events generally lead to longer connected fractures, they typically lead to stronger opening. However, stress redistributions may also lead to the closure of dead ends, or neighboring fractures due to increased compression along the newly connected fracture (illustrated in Figure S1). Therefore, coalescence events (steps in Figure 10) can sometimes lead to a measurable reduction in total fracture area in some cases (e.g., red and orange curves in Figure 8). Finally, the expulsion controls the subsequent closure of the fracture network under the confining stress, due to the reduction of pore pressure after drainage. Note that the decrease in fracture area is not correlated with the amount of expulsed fluid but a result of the reconfiguration of the stresses in the model.

4.3. Fracture Connectivity

Since fracture network connectivity can be expected to have a strong impact on fluid flow, understanding the controlling parameters is especially important. A well-connected, percolating fracture network should also comprise connected fractures from different “rows” and “columns” of the regular grid of initial fractures (cf. Figure 2), since otherwise the connectivity is highly directional.

In the case of random initial orientation, connectivity systematically decreases with increasing stress anisotropy (Figure 10). Strong differential stress leads to pronounced alignment of propagating fractures with the largest principal stress, such that fractures only connect in the vertical direction (Figures 4 and 9a). In contrast, fractures propagate in the direction of their initial orientation when the external stresses are isotropic, leading to a highly interconnected network of fractures in this case (Figure 5). As a result of this effect, the simulations with random initial fracture orientation show highest connectivity of the final fracture network for isotropic and very mildly anisotropic stress (Figure 11, upper graph).

For increasing initial fracture alignment, we observe a shift of the maximum connectivity toward higher differential stresses (Figure 11, middle and lower graphs). A reasonable explanation is that a vertical σ_1 is required to deviate the subhorizontal fractures away from their initial path and create connectivity in the vertical direction (Figure 9b). In other words, the fractures need to rotate to be able to connect to upper and lower neighbors. For very strong differential stresses, however, this rotation may happen quickly, such that again exclusively vertical connections are formed, and the connectivity is directional and low. However, it is noteworthy that although the connectivity for the aligned case under strong differential stress is low

(Figure 10b), Figure 6 shows qualitatively that fractures do connect in different directions. Additionally, we see qualitatively that the fracture traces in this case are highly tortuous, which is also a result of the interplay between initial orientation and subsequent rotation under differential stress (Figure 6). Due to their importance to transport properties, we aim to include additional measures of directional connectivity and tortuosity in future studies.

5. Discussion

5.1. Evolution of Drainage Fracture Networks in Strongly Heated Shale

Improving our understanding of the formation of fracture networks in strongly heated, organic-rich shale requires models that can relate the evolution of a fracture network to the stresses within a rock due to fluid generation and subsequent crack propagation. Our modeling and analysis approach reveals characteristic phases of fracture network evolution in response to the stress state and how each parameter reacts to changing boundary and initial conditions. Adapting some of the parameters used in the laboratory studies of Kobchenko et al. (2014) and extending the analysis by the evolution of propagation angles proved crucial to identify the specific phases of the process (Figures 7–10). Thus, our work provides a numerical tool to quantitatively investigate the evolution of a fracture network in a rock with fast internal fluid generation and overpressure buildup, such as strongly heated shale in the vicinity of magmatic intrusions (e.g., Aarnes et al., 2012; Spacapan et al., 2018).

The present study aims at testing our model against existing knowledge of the process and additionally investigates the effect of varying stress boundary conditions and the orientation of initial fractures. The characteristics of the phases of fracture network evolution as described in the interpretation section are in good agreement with results from previously published laboratory experiments. Based on time-lapse synchrotron imaging of heated, immature shale samples (Kobchenko et al., 2011; Panahi et al., 2018), a three-stage process model was proposed: (1) Fractures initiate from thin kerogen flakes or around elongated pores, then (2) propagate and coalesce, preferentially along lamination planes, but sometimes also obliquely, and (3) finally close under confinement after the hydrocarbons have been expulsed. A similar behavior was documented in analogue experiments analyzing CO_2 production in impermeable, elastic gelatin-yeast-sugar gels, though at a larger model scale, which is more comparable to our numerical setup. Fractures formed at the edges of thin, ellipsoidal gas bubbles, then grew and connected, and finally drained through the boundary and stopped growing (Kobchenko et al., 2013, 2014; Vega & Kovscek, 2019). Similar to the behavior in our numerical results, fluctuations in the fracture area are related to fluid overpressure buildup and relaxation (Kobchenko et al., 2014). Thus, we conclude that our model correctly captures the dynamics of the process and may be used to gain addition quantitative understanding that is not available from experiments. For instance, we are able to extend the understanding of the process by demonstrating the relative importance of crucial parameters such as far-field stress anisotropy, local stress redistributions, and alignment of fractures on the characteristics of the fracture network in each phase. We will address these effects in separate sections below.

5.2. Controls on Fracture Growth and Geometry

Understanding the controlling factors that influence the final fracture network geometry is important, as the geometry controls bulk rock properties such as permeability. The general trend of stronger alignment of propagating fractures in the direction of σ_1 with increasing differential stress (Figures 9 and S3) is expected and represents the dominant control on the final orientation distribution (cf. Teixeira et al., 2017). However, our models yield additional insight into the role of stress interactions between fractures and their effect on fracture coalescence. While fracture tips connecting into walls of neighboring fractures at roughly orthogonal angles tend to stay on their path, two approaching fracture tips are deviated by local stress redistribution and grow into each other after the tips pass each other (Figures 4c, 5c, 6c, and S1). This “embrace” has previously been identified as one of the potential modes of hydraulic fracture coalescence (e.g., Wang, 2016) and is the key to identifying the onset of the overall coalescence phase of the fracture network as a whole (Figure 9). However, the transition might be less clear in real rocks where not all fractures undergo the same phases simultaneously. Qualitatively, similar observations were made in laboratory experiments. The photoelastic properties of gelatin allow visualization of stress fields around the fractures, showing that propagating fracture tips are deviated due to interacting stresses between fractures and that tensile tip stresses vanish upon coalescence (Kobchenko et al., 2014; Vega et al., 2018). However, our numerical results add the benefit of providing a quantitative analysis of the stress state during the coalescence process (cf. Figure S1), which experimental visualization technique does not allow for. Overall, our results emphasize that local stress redistribution may play an important role for fracture coalescence, which influences the connectivity of fractures.

5.3. Controls on Connectivity and Flow Properties

Since fluid expulsion from strongly heated organic-rich shale is mainly controlled by fractures, an important goal is to link fracture network evolution to hydraulic rock properties. In this context, our simulations indicate that differential stress proves important to create higher connectivity in rocks with pronounced layering (Figures 10 and 11). However, the increasing alignment of fractures with the maximum stress direction will likely lead to a strongly anisotropic permeability structure if fractures dominate the fluid flow, especially for strongly anisotropic stress fields. Teixeira et al. (2017) report similar findings using discrete element modeling of shale at the millimeter scale. Under low differential stress, however, our results show that inclined initial flaws can be essential to create fracture connectivity in the vertical direction, since external stresses do not cause rotation of propagating fractures in this direction. This mode of connectivity creation was previously hypothesized by Panahi et al. (2018) but not investigated systematically. Therefore, if the local stress state is not strongly anisotropic, orientation of initial flaws on the microscale may be an important control on the fracture network geometry and thus fluid transport properties. However, since igneous intrusions may cause both local stress perturbations and induce damage due to host rock deformation (Haug et al., 2018; Scheibert et al., 2017; Schmiedel et al., 2019), assessment of realistic boundary and initial conditions is crucial to model the evolving fracture network. Note also that the effects of other parameters such as elastic and strength anisotropy should be investigated in future studies, as they may significantly alter the stress state and direction of propagating fractures.

5.4. Model Limitations

Finally, we will outline some important model limitations. First, the regular grid of fractures in our model setup does not reflect a realistic distribution in a rock, and part of the response might be influenced by the setup, for example, due to a pressure shielding effect of aligned fractures. However, even this simplified setup demonstrates complex fracture interaction phenomena as well as reasonable general trends in the measured parameters and is thus a useful baseline for future realistic setups tuned to investigate specific parameters such as the positioning and density of initial fractures. Additionally, the modeling software ignores the effect of fracture aperture on fracture permeability. Although this may influence flow rates, the coupling between fluid expulsion, opening and closing of fractures, and stress state is included in a physically meaningful way. Importantly, this limitation prevents hydraulic healing of fractures and renewed opening, such that fluid pressures do not build up again. Finally, due to the 2-D nature of our model, additional fracture interactions in the third dimension are not represented. On the other hand, 2-D results are easy to comprehend and visualize and a valuable tool to inform future 3-D studies.

6. Conclusions

In this study, we present a 2-D XFEM numerical model to investigate fracture network evolution in rocks with fast internal fluid generation, overpressure buildup, and expulsion, such as would be expected in strongly heated organic-rich shale close to magmatic intrusions. We integrate analysis of the stress state of the model with tracking of the evolution of specific parameters representing fracture network geometry, including total fracture length, fracture area, connectivity, and propagation angles. Our main conclusions are as follows:

1. The evolution of different fracture network characteristics reveals a three-phase process in our numerical models, comprising (i) initial individual fracture growth dominated by far-field stresses, (ii) interaction and coalescence dominated by local stress redistribution around the fractures, and (iii) fluid expulsion and stress relaxation. This is in good agreement with laboratory experiments at different scales.
2. Magnitude of external stress anisotropy and alignment of the fractures with the largest principal stress direction correlate with the maximum fracture opening.

3. While external stress field configuration controls the main characteristics of the fracture orientation distribution, local stress interactions may cause significant deviations of fracture paths and thus control the coalescence of fractures.
4. In order to create high connectivity in cases with horizontally aligned initial fractures (corresponding to layered rocks), stress anisotropy with $\sigma_V > \sigma_H$ is required. On the other hand, strongly inclined initial fractures are critical for high connectivity if stresses are fully or very nearly isotropic.
5. Strongly anisotropic far-field stresses lead to highly directional connectivity, which may translate to anisotropic fracture permeability.

Data Availability Statement

All data are available from the following repository: https://osf.io/pwjva/ (DOI 10.17605/OSF.IO/PWJVA).

Acknowledgments

We acknowledge funding through the EarthFlows Strategic Research Initiative of the University of Oslo (Universitetet i Oslo) and the Research Council of Norway (Grant no. 267775). We thank geomecon GmbH for access to the numerical code roxol used in this study. We thank Maya Kobchenko for her suggestions for the analysis workflow design.

References

Aarnes, I., Podladchikov, Y., & Svensen, H. (2012). Devolatilization-induced pressure build-up: Implications for reaction front movement and breccia pipe formation. *Geofluids*, *12*(4), 265–279. https://doi.org/10.1111/j.1468-8123.2012.00368.x

Backers, T., C. Gruehser, T. Meier, and G. Dresen (2012), Fracture pattern of borehole breakouts in shale—Comparison of physical and numerical experiments, Paper Presented at 74th EAGE Conference and Exhibition incorporating EUROPEC 2012.

Backers, T., T. Meier, P. Gipper, and O. Stephansson (2015), 2015:30 Technical Note, Rock Mechanics—Assessing the likelihood and extent of fracture growth in the KBS-3 repository at Forsmark, Technical Report Rep., 143 pp.

Belytschko, T., Gracie, R., & Ventura, G. (2009). A review of extended/generalized finite element methods for material modeling. *Modelling and Simulation in Materials Science and Engineering*, *17*(4), 043001. https://doi.org/10.1088/0965-0393/17/4/043001

Bjorlykke, K. (2010). *Petroleum geoscience: From sedimentary environments to rock physics*. Berlin: Springer Science & Business Media. https://doi.org/10.1007/978-3-642-02332-3

Cobbold, P. R., & Rodrigues, N. (2007). Seepage forces, important factors in the formation of horizontal hydraulic fractures and bedding-parallel fibrous veins ('beef' and 'cone-in-cone'). *Geofluids*, *7*(3), 313–322. https://doi.org/10.1111/j.1468-8123.2007.00183.x

Cosenza, P., Ghoreychi, M., De Marsily, G., Vasseur, G., & Violette, S. (2002). Theoretical prediction of poroelastic properties of argillaceous rocks from in situ specific storage coefficient. *Water Resources Research*, *38*(10), 1207. https://doi.org/10.1029/2001WR001201

Dietrich, A. B. (2015), The impact of organic matter on geomechanical properties and elastic anisotropy in the Vaca Muerta shale, Ph.D. Thesis, Colorado School of Mines. Arthur Lakes Library.

Figueroa Pilz, F., Dowey, P. J., Fauchille, A.-L., Courtois, L., Bay, B., Ma, L., et al. (2017). Synchrotron tomographic quantification of strain and fracture during simulated thermal maturation of an organic-rich shale, UK Kimmeridge Clay. *Journal of Geophysical Research: Solid Earth*, *122*, 2553–2564. https://doi.org/10.1002/2016JB013874

Fu, P., Johnson, S. M., & Carrigan, C. R. (2013). An explicitly coupled hydro-geomechanical model for simulating hydraulic fracturing in arbitrary discrete fracture networks. *International Journal for Numerical and Analytical Methods in Geomechanics*, *37*(14), 2278–2300. https://doi.org/10.1002/nag.2135

Galerne, C. Y., & Hasenclever, J. (2019). Distinct degassing pulses during magma invasion in the stratified Karoo Basin—New insights from hydrothermal fluid flow modeling. *Geochemistry, Geophysics, Geosystems*, *20*, 2955–2984. https://doi.org/10.1029/2018GC008120

geomecon (2019), roxol—The fracture network evolution simulator [Computer software], retrieved from www.roxol.de

Haug, Ø. T., Galland, O., Souloumiac, P., Souche, A., Guldstrand, F., Schmiedel, T., & Maillot, B. (2018). Shear versus tensile failure mechanisms induced by sill intrusions: Implications for emplacement of conical and saucer-shaped intrusions. *Journal of Geophysical Research: Solid Earth*, *123*, 3430–3449. https://doi.org/10.1002/2017JB015196

Iyer, K., Schmid, D. W., Planke, S., & Millett, J. (2017). Modelling hydrothermal venting in volcanic sedimentary basins: Impact on hydrocarbon maturation and paleoclimate. *Earth and Planetary Science Letters*, *467*, 30–42. https://doi.org/10.1016/j.epsl.2017.03.023

Jaeger, J. C., Cook, N. G., & Zimmerman, R. (2009). *Fundamentals of rock mechanics*. New York: John Wiley & Sons.

Jin, Z. H., & Johnson, S. E. (2008). Primary oil migration through buoyancy-driven multiple fracture propagation: Oil velocity and flux. *Geophysical Research Letters*, *35*, L09303. https://doi.org/10.1029/2008GL033645

Jin, Z.-H., Johnson, S. E., & Fan, Z. Q. (2010). Subcritical propagation and coalescence of oil-filled cracks: Getting the oil out of low-permeability source rocks. *Geophysical Research Letters*, *37*, L01305. https://doi.org/10.1029/2009GL041576

Kobchenko, M., Hafver, A., Jettestuen, E., Galland, O., Renard, F., Meakin, P., et al. (2013). Drainage fracture networks in elastic solids with internal fluid generation. *EPL (Europhysics Letters)*, *102*(6), 66002. https://doi.org/10.1209/0295-5075/102/66002

Kobchenko, M., Hafver, A., Jettestuen, E., Renard, F., Galland, O., Jamtveit, B., et al. (2014). Evolution of a fracture network in an elastic medium with internal fluid generation and expulsion. *Physical Review E*, *90*(5), 052801. https://doi.org/10.1103/PhysRevE.90.052801

Kobchenko, M., Panahi, H., Renard, F., Dysthe, D. K., Malthe-Sørenssen, A., Mazzini, A., et al. (2011). 4D imaging of fracturing in organic-rich shales during heating. *Journal of Geophysical Research*, *116*, B12201. https://doi.org/10.1029/2011JB008565

Lecampion, B., Bunger, A., & Zhang, X. (2018). Numerical methods for hydraulic fracture propagation: A review of recent trends. *Journal of Natural Gas Science and Engineering*, *49*, 66–83. https://doi.org/10.1016/j.jngse.2017.10.012

Marquez, X. M., & Mountjoy, E. W. (1996). Microfractures due to overpressures caused by thermal cracking in well-sealed Upper Devonian reservoirs, deep Alberta Basin. *AAPG Bulletin*, *80*(4), 570–588.

Mischo, H., and T. Backers (2012), Analysis of fracture coalescence by fracture mechanics numerical simulation, Paper Presented at ISRM International Symposium-EUROCK 2012, International Society for Rock Mechanics and Rock Engineering.

Ougier-Simonin, A., Renard, F., Boehm, C., & Vidal-Gilbert, S. (2016). Microfracturing and microporosity in shales. *Earth-Science Reviews*, *162*, 198–226. https://doi.org/10.1016/j.earscirev.2016.09.006

Panahi, H., Kobchenko, M., Meakin, P., Dysthe, D. K., & Renard, F. (2018). In-situ imaging of fracture development during maturation of an organic-rich shale: Effects of heating rate and confinement. *Marine and Petroleum Geology*, *95*, 314–327. https://doi.org/10.1016/j.marpetgeo.2018.05.002

Panahi, H., Kobchenko, M., Meakin, P., Dysthe, D. K., & Renard, F. (2019). Fluid expulsion and microfracturing during the pyrolysis of an organic rich shale. *Fuel*, *235*, 1–16. https://doi.org/10.1016/j.fuel.2018.07.069

Sanderson, D. J., & Nixon, C. W. (2018). Topology, connectivity and percolation in fracture networks. *Journal of Structural Geology*, *115*, 167–177. https://doi.org/10.1016/j.jsg.2018.07.011

Scheibert, J., Galland, O., & Hafver, A. (2017). Inelastic deformation during sill and laccolith emplacement: Insights from an analytic elastoplastic model. *Journal of Geophysical Research: Solid Earth*, *122*, 923–945. https://doi.org/10.1002/2016JB013754

Schmiedel, T., Galland, O., Haug, Ø. T., Dumazer, G., & Breitkreuz, C. (2019). Coulomb failure of Earth's brittle crust controls growth, emplacement and shapes of igneous sills, saucer-shaped sills and laccoliths. *Earth and Planetary Science Letters*, *510*, 161–172. https://doi.org/10.1016/j.epsl.2019.01.011

Schön, J. H. (2015). *Physical properties of rocks: Fundamentals and principles of petrophysics*. New York: Elsevier.

Spacapan, J., Palma, J., Galland, O., Manceda, R., Rocha, E., D'Odorico, A., & Leanza, H. (2018). Thermal impact of igneous sill-complexes on organic-rich formations and implications for petroleum systems: A case study in the northern Neuquén Basin, Argentina. *Marine and Petroleum Geology*, *91*, 519–531. https://doi.org/10.1016/j.marpetgeo.2018.01.018

Spacapan, J. B., D'Odorico, A., Palma, O., Galland, O., Rojas Vera, E., Ruiz, R., et al. (2020). Igneous petroleum systems in the Malargüe fold and thrust belt, Río Grande Valley area, Neuquén Basin, Argentina. *Marine and Petroleum Geology*, *111*, 309–331. https://doi.org/10.1016/j.marpetgeo.2019.08.038

Spacapan, J. B., D'Odorico, A., Palma, O., Galland, O., Senger, K., Ruiz, R., et al. (2019). Low resistivity zones at contacts of igneous intrusions emplaced in organic-rich formations and their implications on fluid flow and petroleum systems: A case study in the northern Neuquén Basin, Argentina. *Basin Research*, *32*(1), 3–24. https://doi.org/10.1111/bre.12363

Stöckhert, F. (2015), Fracture mechanics applied to hydraulic fracturing in laboratory experiments, Ruhr-Universität Bochum.

Teixeira, M. G., Donzé, F., Renard, F., Panahi, H., Papachristos, E., & Scholtès, L. (2017). Microfracturing during primary migration in shales. *Tectonophysics*, *694*, 268–279. https://doi.org/10.1016/j.tecto.2016.11.010

Townsend, M. R. (2018). Modeling thermal pressurization around shallow dikes using temperature-dependent hydraulic properties: Implications for deformation around intrusions. *Journal of Geophysical Research: Solid Earth*, *123*, 311–323. https://doi.org/10.1002/2017JB014455

Vega, B., & Kovscek, A. R. (2019). A systematic study of internal gas generation in shale source rocks using analog experiments. *Journal of Petroleum Science and Engineering*, *173*, 209–221. https://doi.org/10.1016/j.petrol.2018.10.006

Vega, B., J. Yang, H. A. Tchelepi, and A. R. Kovscek (2018), Investigation of stress field and fracture development during shale maturation using analog rock systems, Paper Presented at SPE Annual Technical Conference and Exhibition, Society of Petroleum Engineers.

Vernik, L. (1994). Hydrocarbon-generation-induced microcracking of source rocks. *Geophysics*, *59*(4), 555–563. https://doi.org/10.1190/1.1443616

Wang, H. (2016). Numerical investigation of fracture spacing and sequencing effects on multiple hydraulic fracture interference and coalescence in brittle and ductile reservoir rocks. *Engineering Fracture Mechanics*, *157*, 107–124. https://doi.org/10.1016/j.engfracmech.2016.02.025

Witherspoon, P. A., Wang, J. S. Y., Iwai, K., & Gale, J. E. (1980). Validity of cubic law for fluid flow in a deformable rock fracture. *Water Resources Research*, *16*(6), 1016–1024. https://doi.org/10.1029/WR016i006p01016

Zanella, A., Cobbold, P. R., Ruffet, G., & Leanza, H. A. (2015). Geological evidence for fluid overpressure, hydraulic fracturing and strong heating during maturation and migration of hydrocarbons in Mesozoic rocks of the northern Neuquén Basin, Mendoza Province, Argentina. *Journal of South American Earth Sciences*, *62*, 229–242. https://doi.org/10.1016/j.jsames.2015.06.006